

Resonate and Fire Neuron with Fixed Magnetic Skyrmions

Md. Ali Azam¹, Dhritiman Bhattacharya¹, Damien Querlioz², Jayasimha Atulasimha^{1,3,*}

1. Department of Mechanical and Nuclear Engineering, Virginia Commonwealth University.
2. Centre de Nanosciences et de Nanotechnologies, CNRS, Univ Paris-Sud, Université Paris-Saclay, 91405 Orsay France.
3. Department of Electrical and Computer Engineering, Virginia Commonwealth University.
*jatulasimha@vcu.edu

Abstract: In the brain, the membrane potential of many neurons oscillates in a subthreshold damped fashion and fire when excited by an input frequency that nearly equals their eigen frequency. In this work, we investigate theoretically the artificial implementation of such “resonate-and-fire” neurons by utilizing the magnetization dynamics of a fixed magnetic skyrmion in the free layer of a magnetic tunnel junction (MTJ). To realize firing of this nanomagnetic implementation of an artificial neuron, we propose to employ voltage control of magnetic anisotropy or voltage generated strain as an input (spike or sinusoidal) signal, which modulates the perpendicular magnetic anisotropy (PMA). This results in continual expansion and shrinking (i.e. breathing) of a skyrmion core that mimics the subthreshold oscillation. Any subsequent input pulse having an interval close to the breathing period or a sinusoidal input close to the eigen frequency drives the magnetization dynamics of the fixed skyrmion in a resonant manner. The time varying electrical resistance of the MTJ layer due to this resonant oscillation of the skyrmion core is used to drive a Complementary Metal Oxide Semiconductor (CMOS) buffer circuit, which produces spike outputs. By rigorous micromagnetic simulation, we investigate the interspike timing dependence and response to different excitatory and inhibitory incoming input pulses. Finally, we show that such resonate and fire neurons have potential application in coupled nanomagnetic oscillator based associative memory arrays.

I. Introduction

Following the pioneering vision of Carver Mead [1], neuromorphic computing has garnered considerable interest in recent times due to its potential advantage in dealing with computational problems with ill conditioned input data, adaptive nature of these systems to mitigate the effect of component failure and efficiency compared to fully Boolean logic based computation [2–5]. Due to the complex and mixed analog-digital nature of the brain, a major hurdle towards developing neuromorphic computation platforms has been finding materials and devices to mimic brain like behavior and developing architectures based on such systems. Current hardware artificial neural networks are mostly implemented with purely CMOS circuits and require large number of components to ensure robustness [3,6]. This poses a major challenge for the scaling and energy efficiency of neuromorphic computation.

Nanomagnetic devices are one of the promising alternatives to implement neuromorphic computing and other non-von-Neumann like architectures due to their low energy consumption, nonlinear dynamics, and non-volatility. Many nanomagnetic devices that can potentially form the building blocks of neuromorphic computing: artificial neurons and synapses, have been proposed [4,7–14]. Among artificial neurons, most emulate the behavior of (leaky) integrate and fire type neurons [3,10]. In an integrate and fire type neuron, the membrane potential increases in response to an input spike and fires if it reaches a certain threshold [15]. Therefore, the firing frequency depends only on the strength of the stimulus. However, in the brain, many neurons also feature damped or sustained subthreshold oscillation [16–19] of membrane potential. Such neurons therefore show sensitivity towards the timing of stimulus. Consequently, a strong stimulus may not produce a spiking output if the incoming stimulus is not in phase with the oscillation of membrane potential, thus providing an inhibitory function. It also leads to many interesting phenomena such as fluctuation of spiking

probability and selective communication [20]. Such “resonate-and-fire” neurons could also be useful in different neural networks where computation involves synchronized oscillation of several spin torque nanosensors (SNTOs) for pattern recognition [21]. Such networks come in different versions: for example, in ref. [21] patterns are encoded by frequency-shift keying (FSK) whereas in most other work [22–24] patterns are encoded with phase shift keying (PSK), but all of them could benefit from circuits able to detect synchrony through resonance.

In this work, we investigate the implementation of an artificial resonate-and-fire neuron by utilizing the magnetization dynamics of a fixed magnetic skyrmion in the free layer of a magnetic tunnel junction. Magnetic skyrmions (Fig. 1 (a)) are topologically protected spiral spin textures [25,26], which can be translated by applying small current [27,28] or reversed (in patterned dots) using a small voltage that controls the magnetic anisotropy [29,30]. Until now, this behavior has been leveraged to propose logic and memory devices based on magnetic skyrmions [31–35].

While nanomagnetic device based integrate and fire type neurons have been studied extensively, the resonate and fire type neuron proposed using nanomagnetic devices in this work, is unique to this paper and would be essential to compare the synchronization in arrays of nanomagnetic oscillators as described above for applications such as pattern recognition. While various schemes mimicking neuron and synapse activities have also been proposed utilizing current induced motion of skyrmions [36–39], neuromorphic devices based on moving skyrmions could have a large foot print and are dissipative as they use current to move the skyrmions. We previously proposed nanomagnetic memory devices utilizing voltage control of fixed magnetic skyrmions in the free layer of a MTJ structure [29,40,41] that can alleviate these issues. In this paper, we use such a voltage control of a fixed skyrmion based scheme to achieve the functionality of resonate and fire neurons.

The next section describes two “resonate and fire” neuron devices based on the novel mechanism of resonant oscillations of a skyrmion core due to voltage control of anisotropy: direct voltage control of magnetic anisotropy (VCMA) and strain mediated voltage control of anisotropy in magnetostrictive materials. This is followed by a section explaining the modeling of voltage induced magnetization dynamics, followed by a discussion of skyrmion core oscillation, resonant behavior and application of the “resonate and fire” functionality for detection of phase and frequency synchronization.

II. Device:

Our proposed device is a MTJ structure in which the circular free layer hosts a fixed skyrmion. We propose two different devices where application of a voltage modulates the perpendicular anisotropy of the free layer through two different physical mechanisms. The anisotropy can be modulated via voltage control of magnetic anisotropy [42–44] in the device shown in Figure 1(b) and voltage generated strain [45,46] in the device shown in Figure 1(c). Modulation of perpendicular anisotropy in the system induces breathing of skyrmions. In other words, the skyrmion core increases and decreases in size. This mimics the subthreshold damped oscillations of resonate and fire neurons. The electrical resistance of the MTJ layer (R_2) depends on the magnetization orientation of the free layer (i.e. the size of the skyrmion core) relative to that of the fixed layer. For the sake of explanation, let us assume that the orientation of the magnetization of the fixed layer is antiparallel with respect to the one of the skyrmion core. As the skyrmion core expands during the breathing, more spins in the free layer will be antiparallel with respect to the fixed layer spins. Therefore, the resistance of the MTJ structure will increase. We thus propose to use a voltage divider consisting of a fixed resistor and the voltage controlled MTJ resistance to drive a CMOS buffer from OFF to ON state as shown in Fig 1.

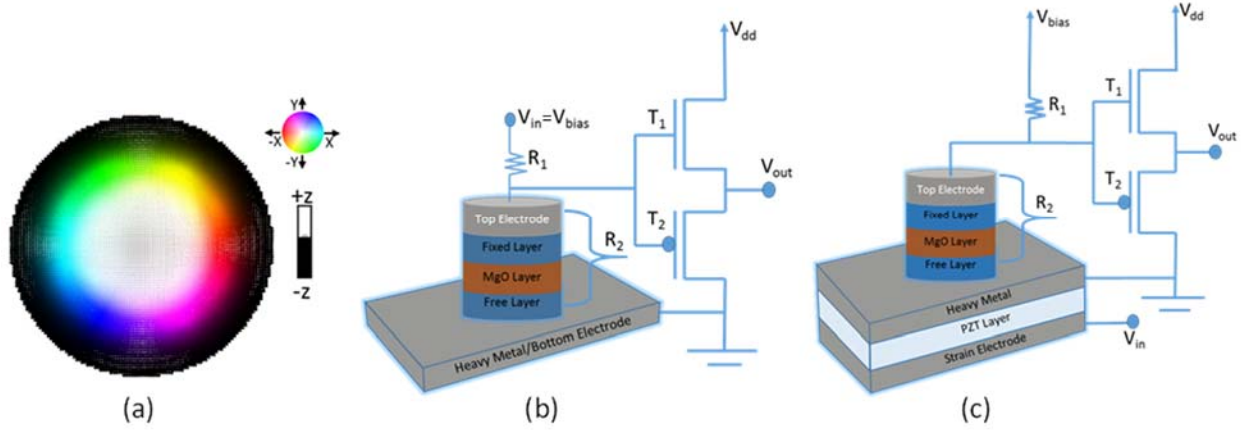


Figure 1. (a) A core-up skyrmion, color code on the right shows the direction of the spin, (b) Proposed device structure operated with voltage control of magnetic anisotropy (VCMA) (c) MTJ structure stacked on PZT layer for strain control of magnetic anisotropy. Note that, CMOS buffer is driven by the MTJ resistance. Therefore, fixed layer magnetization needs to be opposite to that of skyrmion core.

If the resistance of the MTJ stack increases during skyrmion expansion, potential drop across the MTJ resistance (R_2) will be higher. We can choose the ratio between R_1 and R_2 such that, at a given threshold this increase causes the transistor T_1 to be turned on and generate a firing pulse. (NOTE: A similar behavior can be achieved by choosing the fixed layer magnetization orientation to be parallel with respect to the magnetization orientation of the skyrmion core and driving the CMOS buffer by the potential drop across resistance R_1). In short, if the skyrmion core size increases beyond a threshold, potential drop across the MTJ stack will produce an input voltage to the CMOS circuit that will exceed the threshold voltage, causing the buffer to “fire”, i.e. produce a high output. In ref. [47] resistance-area product of MTJ was found to be in the range of $225\text{-}650 \text{ } \Omega \cdot \mu\text{m}^2$ and typical tunnel magneto-resistance ratio between parallel and antiparallel configuration is 100% [47]. However, in this case, magnetization is oscillating between a skyrmionic state and a quasi-antiparallel state. Typical CMOS buffer have gating voltage in the range of 1 V. Hence, we can design a bias voltage (V_{bias}) and appropriate ratio for R_1 to R_2 . It would be preferable to maximize R_1 and R_2 (to minimize standby power dissipation due to V_{bias}) while ensuring reasonable RC time constant for resonant operation of the device. In this work, for the sake of simplicity, we do not model the magnetoresistance change due to skyrmion breathing and the circuit dynamics of the CMOS buffer. In other words, in Fig 1 (corresponding to both device implementations for the resonate and fire neuron), we only model the magnetization dynamics of the skyrmions and set a threshold value of average magnetization along the z-axis ($m_{z_threshold}=0.8$, magnetization is almost antiparallel to the free layer). For $m_{z_free} > m_{z_threshold}$, we consider the CMOS buffer to be in the ‘ON’ or “high” state and “OFF” or “low” otherwise. This naturally gives rise to a firing output.

III. Methods

Micromagnetic simulation software MuMax3 [48] was used to perform the simulations where the magnetization dynamics is found by solving the Landau-Lifshitz-Gilbert (LLG) equation,

$$\frac{\partial \vec{m}}{\partial t} = \vec{\tau} = \left(\frac{-\gamma}{1+\alpha^2} \right) \left(\vec{m} \times \vec{H}_{eff} + \alpha \left(\vec{m} \times (\vec{m} \times \vec{H}_{eff}) \right) \right) \quad (1)$$

where \vec{m} is the reduced magnetization (\vec{M}/M_s), M_s is the saturation magnetization, γ is the gyromagnetic ratio and α is the Gilbert damping coefficient. The effective magnetic field \vec{H}_{eff} is given by,

$$\vec{H}_{eff} = \vec{H}_{demag} + \vec{H}_{exchange} + \vec{H}_{anis} + \vec{H}_{thermal} \quad (2)$$

Here, \vec{H}_{demag} is the effective field due to demagnetization energy, $\vec{H}_{exchange}$ is the effective field due to Heisenberg exchange coupling and Dzyaloshinskii-Moriya Interaction (DMI). The DMI contribution to $\vec{H}_{exchange}$ is given by [48]:

$$\vec{H}_{DM} = \frac{2D}{\mu_0 M_s} \left[\frac{\partial m_z}{\partial x}, \frac{\partial m_z}{\partial y}, -\frac{\partial m_x}{\partial x} - \frac{\partial m_y}{\partial y} \right] \quad (3)$$

where m_z is the z-component of magnetization and D is the effective DMI constant.

The effective field due to the perpendicular anisotropy, \vec{H}_{anis} , is expressed as [48],

$$\vec{H}_{anis} = \frac{2K_{u1}}{\mu_0 M_s} (\vec{u} \cdot \vec{m}) \vec{u} + \frac{4K_{u2}}{\mu_0 M_s} (\vec{u} \cdot \vec{m})^3 \vec{u} \quad (4)$$

where K_{u1} and K_{u2} are first and second order uniaxial anisotropy constants and \vec{u} is the unit vector in the direction of the anisotropy (i.e. perpendicular anisotropy in this case). VCMA/strain effectively modulates the anisotropy energy density. The resultant change in uniaxial anisotropy due to VCMA/strain is incorporated by modulating K_{u1} while keeping $K_{u2} = 0$. For VCMA, this change is given by $\Delta k_{u1} = \Delta PMA = aE$. Here, a and E are respectively the coefficient of electric field control of magnetic anisotropy and the applied

Parameters	Value
Saturation Magnetization (M_{sat})	1×10^6 A/m
Exchange Constant (A_{ex})	2×10^{-11} J/m
Perpendicular Anisotropy Constant (K_{u1})	6×10^5 J/m ³
Gilbert Damping (α)	0.03
DMI Constant (D)	3 mJ/m ²

electric field. On the other hand, for strain, this is given by $\Delta k_{u1} = \Delta PMA = \frac{3}{2} \lambda \sigma$, where λ and σ are respectively the magnetostriction coefficient and the applied stress.

In order to reduce the effect of VCMA/strain on the fixed layer, the thickness of the fixed layer can be made lower compared to that of the free layer. This lower thickness ensures a high perpendicular magnetic anisotropy. Materials with low VCMA/magnetostriction co-efficient can be chosen for the fixed layer so that effect of voltage application is minimal. Additionally, one can use a synthetic antiferromagnetic [49] layer to increase magnetic stability of the fixed layer. These ensure the magnetization of the fixed magnetic layer does not rotate much due to VCMA or due to strain (if any) transferred to it. Therefore, we only simulate the magnetization dynamics of the free layer. The synthetic antiferromagnetic layer also offsets the dipolar interaction between the fixed and the free layer. Hence, we ignore anti-symmetric modification effects due to dipolar effects in our model. Exchange interaction and DMI can be modulated when an electric field is applied. However, these effects are minimal [41] and will only result in a small change in the breathing frequency and will not change the key results of our work significantly.

IV. Results

A. Damped Oscillatory Behavior of Skyrmions

We simulated the magnetization dynamics in a 100 nm diameter nanodisk with thickness of 1 nm. Our geometry was discretized into $1 \times 1 \times 1 \text{ nm}^3$ cells. Using the parameter values in table I, the ground magnetization state was found to be a skyrmion. A triangular input spike of $\Delta\text{PMA}=1 \times 10^5 \text{ J/m}^3$ was applied with 50 ps rise and 50 ps fall time (NOTE: We use fast rise and fall time in the triangular pulse to simulate response to a near ideal pulse whereas sinusoidal inputs are used later for more realistic device simulations). Furthermore, we are mostly interested in frequency or phase synchronization of sinusoidal waveforms, but nevertheless choose triangular spikes initially due to similarity to actual spike like stimulus available in real neurons (though time scales for biological and artificial skyrmions resonate and fire neurons are vastly different). The momentary change in anisotropy causes the core of the skyrmions to expand and oscillate about the equilibrium state.

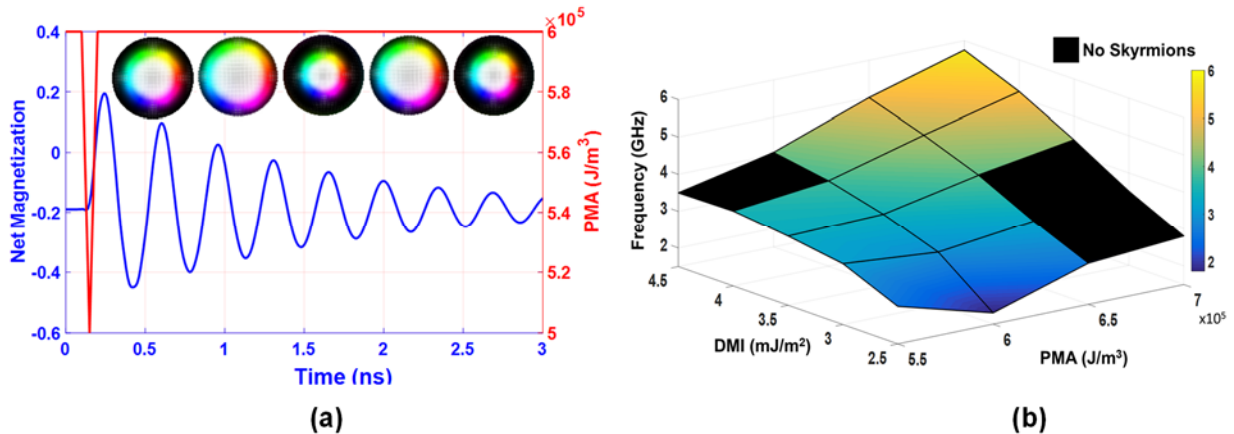


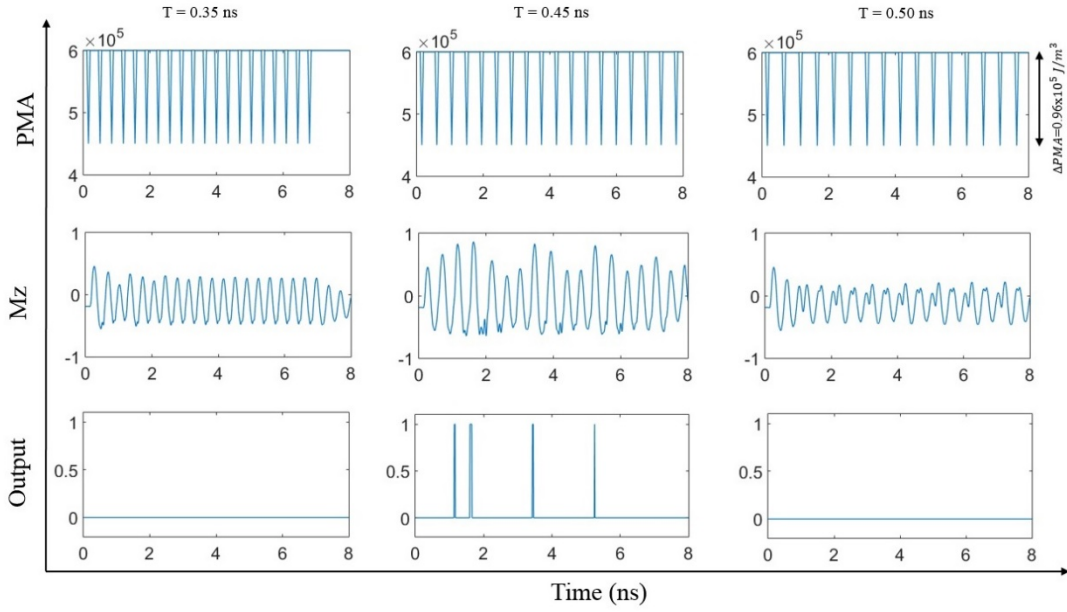
Figure 2. (a) Damped oscillation of a fixed skyrmion's core due to stimulation with a single pulse [Red color line: Input spike, Blue color line: Output average magnetization along the perpendicular direction (z-axis) (b) Modulation of breathing frequency by varying the interfacial parameters.

The oscillatory behavior can be seen from the net magnetization curve in Figure 2 (a). This imitates the subthreshold neuron oscillation of a resonant neuron. From this magnetization dynamics, the breathing frequency of the skyrmion can be determined. This is analogous to the eigen frequency (i.e. damped oscillation frequency) of the neuron. This information is important as an input spike train or sinusoid should have a frequency that nearly equals the eigen frequency to cause a neuron to resonate and spike. This breathing frequency strongly depends on the parameters of the system. Here, we determine the breathing frequency as a function of interfacial parameters PMA and DMI (Fig. 2 (b)). This frequency can be easily tuned in the range of 1.8 GHz to 5.75 GHz. In addition to interfacial parameters, one can use a DC bias voltage to change the PMA which will subsequently tune the frequency about which the skyrmion oscillates but this is not discussed here as it is beyond the scope of this paper.

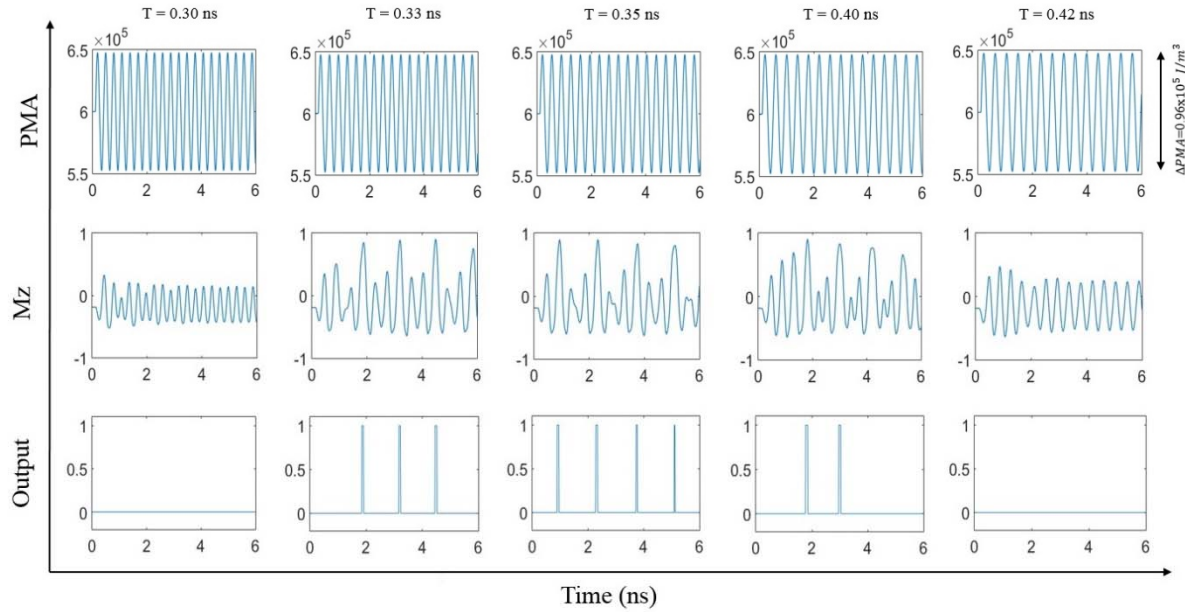
B. Resonant behavior of Skyrmions

The skyrmion breathing frequency estimated in the last sub-section is now utilized to drive the skyrmion into resonance and show the resonate and fire behavior is very sensitive to this excitation frequency. We again start with triangular input pulses for reasons mentioned in the prior sub-section. Triangular pulses of $\Delta\text{PMA}=1.5 \times 10^5 \text{ J/m}^3$ of time interval in a range of 0.35-0.50 ns was applied to the system. At the PMA chosen (in the absence of voltage applied) the core had a breathing frequency of approximately 2.86 GHz ($T=0.35 \text{ ns}$). Skyrmion breathing of significant amplitude was observed when two input spikes were separated by an interval that falls in the range 0.43 ns to 0.46 ns. Breathing with diminishing amplitude was

observed in other cases. The example in Fig. 3(a) shows cases for 3 different time intervals between two successive input spikes: 0.35 ns, 0.45 ns and 0.50 ns.



(a)



(b)

Figure 3. Resonant behavior: (a) Spike input (b) sinusoidal input

Considering $M_{z_threshold}=0.8$, a spiking output can be found for time interval of 0.45 ns, while no output spikes are found when the time interval was 0.35 ns and 0.50 ns. Other than the dependency on time interval the skyrmion core resonance is significantly sensitive to the amplitude of the input impulse. Lowering ΔPMA to $1.4 \times 10^5 \text{ J/m}^3$ failed to produce any output as expected due to sub-threshold oscillation. However, increasing the ΔPMA to $1.75 \times 10^5 \text{ J/m}^3$ lowered (instead of increasing) the firing rate from 4 for first 10 ns

to just 2. This is because we consider M_z threshold=0.8, which occurs when ~80% of the spins point upwards. As the core size is very large, peripheral (boundary) effects strongly influence the breathing dynamics which makes the behavior strongly nonlinear. Due to this, the correlation between the change of input magnitude and the spiking behavior is hard to predict at these limits. Hence, for triangular input with $T=0.45\text{ns}$, ΔPMA of $1.5 \times 10^5 \text{ J/m}^3$ resulted in the best firing behavior.

While triangular spikes were used to illustrate the spiking behavior, a sinusoidal input pulse is more useful for many practical applications. Appropriate frequency sinusoidal inputs can also result in firing due to the same principle, i.e. a sinusoid of given amplitude, whose frequency is resonant with the eigen frequency produces the strongest spiking behavior. Sinusoids of different frequencies with peak to peak $\Delta PMA=0.96 \times 10^5 \text{ J/m}^3$ were used as inputs. Strongest firing (4 spikes over 6 ns) was found around 2.86 GHz (time period of 0.35 ns) input frequency. Higher frequency (3 GHz or time period of 0.33 ns) and lower frequency (2.5 GHz or time period of 0.4 ns) resulted in weaker spiking behavior (less than 4 spikes over the same 6 ns). Further deviation in frequency from resonance: 3.3 GHz (time period of 0.3 ns) and 2.38 GHz (time period of 0.42 ns) resulted in no spiking behavior at all.

We note that the eigen frequency (for single triangular pulse) and resonant frequency for triangular and sinusoidal inputs all appear to be different. This is because the ΔPMA produced by the input voltage leads to a variation in the net PMA experienced by the breathing skyrmion, which in turn changes its frequency.

The change in perpendicular anisotropy is given by $\Delta PMA = aE$. The VCMA co-efficient was found to be as large as 290 fJ/Vm experimentally[50] and 1800 fJ/Vm theoretically[51]. Using $a= 100 \text{ fJ/Vm}$, peak to peak $\Delta PMA=0.96 \times 10^5 \text{ J/m}^3$ can be achieved using a peak voltage of 0.48 V, considering the MgO layer to be of 1 nm thickness. Energy dissipation per cycle will be $\frac{1}{2}CV^2$ considering energy dissipation is dominated by the energy required to charge the capacitive MgO layer. The capacitance of the MgO layer $C= 0.487 \text{ fF}$ for relative permittivity of 7 [52]). This translates into an energy dissipation of 56 aJ.

On the other hand, change in PMA achieved via strain is given by $\Delta PMA = \frac{3}{2} \lambda \sigma$. Magnetostrictive coefficient λ is 37 ppm for CoFeB [53]. Stress cycles with magnitude ~1 GPa will be needed to drive this system to resonance, which is not practical. Materials with higher magnetostrictive coefficients exist. For example, FeGa has a coefficient of 300 ppm [54] while λ can be as high as 1000 ppm for Terfenol-D [55,56]. The requirement of stress will be correspondingly lower (respectively ~167 MPa and ~50MPa) assuming that such material systems with such highly magnetostrictive materials also exhibit DMI (has not been studied so far). To generate 50 MPa stress, required voltage is 83.375 mV. We again consider energy dissipation is dominated by the energy required to charge the capacitive piezoelectric layer. The relative permittivity of the piezoelectric layer is taken to be 1000. Considering 100 nm thick PZT layer, capacitance $C=0.695 \text{ fF}$. This gives rise to an energy dissipation of mere 2.4 aJ.

We note that, energy dissipation ~ femto-Joules (fJ) in the resistive elements (due to V_{bias}) will dominate energy dissipated in the scaled MTJ (~10-100 aJ) as well as the CMOS buffer (each CMOS device typically require ~100 aJ per switching event [57]). Thus, the total energy requirement will be ~ femto-Joule/spiking event.

These values are highly attractive in comparison to a purely CMOS implementation of the resonate and fire neuron. In reference [58], CMOS implementation of a resonate-and-fire neuron involves capacitors approaching pico-Farad, leading to an energy consumption per firing event in the range of pico-Joules, an area of many micrometer square and resonant frequency of a few 10s of Hz. In fact, the proposed hybrid skyrmion-MTJ and CMOS buffer implementation of the resonate and fire neuron, is capable of resonant frequencies ~few GHz and is potentially 3 orders of magnitude more energy efficient/spiking event and

potentially has 2 orders of magnitude higher density than that the all CMOS implementation [58] as shown in Table 1.

Table 1. Performance comparison of proposed hybrid nanomagnet-CMOS vs. all CMOS resonate and fire neuron [58].

Performance metric	Hybrid fixed skyrmion-MTJ and CMOS buffer	All CMOS [58]
Energy dissipation/spiking event	~ femto-Joule	~pico-Joule
Density (area per device)	~0.01 micron ²	~micron ²
Resonance frequency	~ GHz	~10s Hz (can be designed to be much faster)

C. Frequency and Phase synchronization detection of STNO oscillators

Frequency and phase synchronization detection of coupled spin torque nano-oscillators (STNO) is an important component is neuromorphic computing schemes that implement associative memory[22–24]. In this section, we show that our proposed device can be used to detect phase and frequency synchronization of STNOs and, in general, any coupled oscillators. In this subsection, we consider the outputs of two STNOs (or two coupled oscillators) in general have been added together as:

$$V = V \sin(2\pi f_1 + \phi_1) + V \sin(2\pi f_2 + \phi_2)$$

Here f_1 (f_2) and ϕ_1 (ϕ_2) are respectively the frequency and phase of the first and second oscillator output.

Case I: Phase differs, frequency synchronized

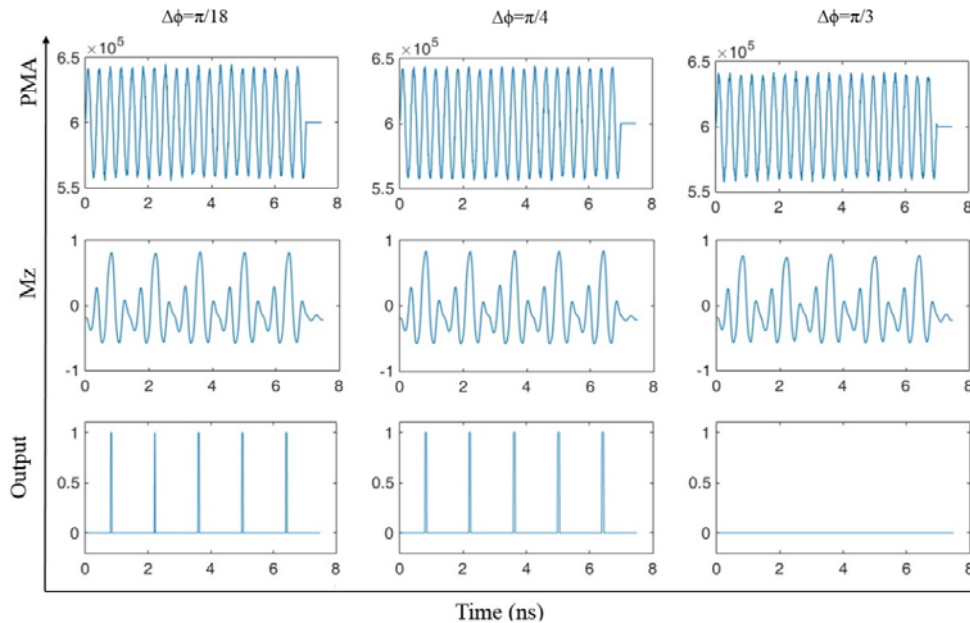


Figure 4. Phase detection: As the phase difference increases the amplitude of the input decreases thus making it harder for the magnetization to reach the threshold limit for firing

Here the two signals have no difference in frequency but have a phase difference ($\Delta\phi$) of $\pi/18$ (10°), $\pi/4$ (45°), $\pi/3$ (60°). We also include a random phase noise as follows:

$$\phi_1 = \phi_{10} + \phi_{random,1}$$

$$\phi_2 = \phi_{20} + \phi_{random,2}$$

$$\Delta\phi = \phi_1 - \phi_2$$

The random phase noise added here is white noise. In figure 4 we show that output spikes several times when the phase difference is below a certain limit (e.g. 45° and below) and when the phase difference is larger (60°) the output fails to spike.

Case II: Frequency differs, (we assume that at $t=0$, $\Delta\phi = 0$)

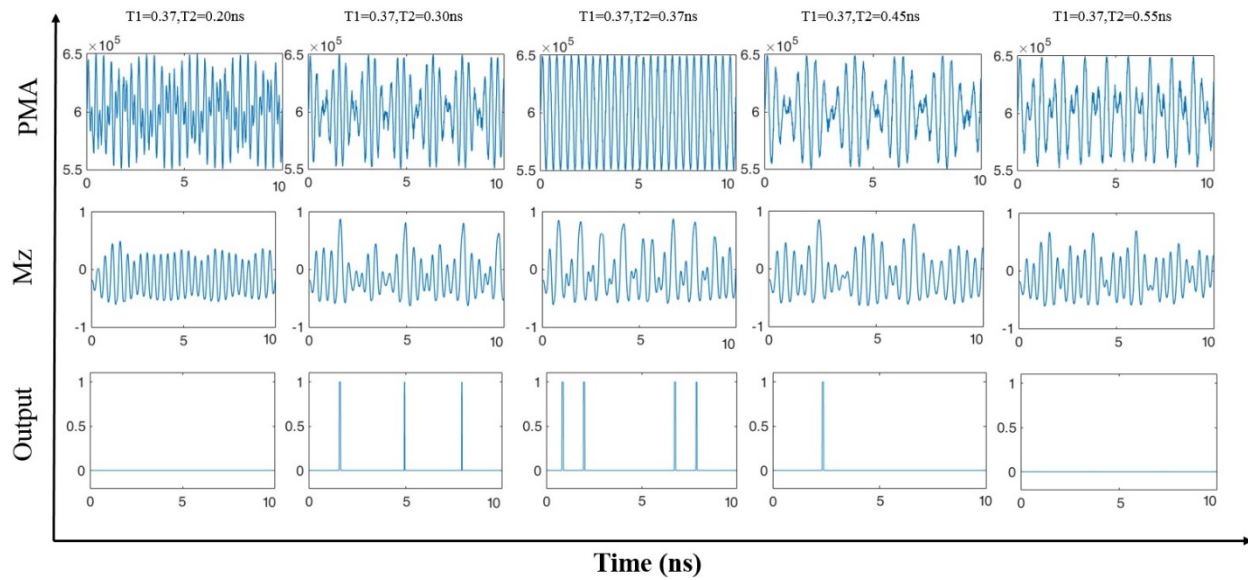


Figure 5. Frequency synchronization detection

Here the two signals have different frequency but have no phase difference at $t=0$. Both signals are subjected to phase noise and the spiking output is analyzed over 10 ns. A signal with a frequency of 2.7 GHz ($T=0.37$ ns) is chosen as the base signal. This frequency is slightly lower than the actual resonance frequency (2.86GHz) and intentionally chosen so to demonstrate robustness of the frequency synchronization detection to frequencies that are slightly off resonance. Successive signals added to it have frequencies of 5 GHz, 3.33 GHz, 2.7 GHz, 2.22 GHz and 1.82 GHz. When both frequencies are equal (2.7 GHz) 4 spikes are produced in 10 ns; when mismatched by $\sim 20\%$ (e.g. the 3.33 GHz and 2.22 GHz cases), less than 4 spikes are produced in 10 ns and finally with significant deviation (e.g. 5 GHz and 1.82 GHz) no output spike is produced. This suggests that further investigation into the skyrmion magnetization

dynamics may reveal an appropriate input amplitude (and other conditions) where the number of output spikes over a given time window can provide an estimate of the degree of synchronization.

V. Conclusion

In this work, we studied novel nonlinear resonant dynamics of the core of a fixed skyrmion and showed that it has potential to lead to an energy efficient hybrid voltage controlled nanomagnetic device – CMOS device based circuit that can implement a “resonate and fire” neuron. The energy dissipation of such a device per spiking event can potentially be ~femto-Joules, which is 3 orders of magnitude (1000 times) less than an all CMOS implementation [58]. It can scale to much higher densities (~100 times less area) than an all CMOS implementation [58], while being able to exhibit resonance frequencies in the range of a few Giga-Hertz

Furthermore, future work on combining such voltage controlled nanomagnetic frequency and phase synchronization detectors with voltage controlled nanomagnetic oscillators (not discussed in detail this paper) can lead to all voltage controlled-nanomagnetic devices (with some CMOS devices) based neuromorphic circuits that are potentially very energy efficient, dense and fast.

Acknowledgement: M.A.A., D.B. and J.A. are supported in part by the National Science Foundation CAREER grant CCF-1253370, Virginia Microelectronics Seed Grant, Virginia Quest Commercialization Grant.

REFERENCES

- [1] Mead C 1990 Neuromorphic Electronic Systems *Proc. IEEE* **78** 1629–36
- [2] Indiveri G and Liu S C 2015 Memory and Information Processing in Neuromorphic Systems *Proc. IEEE* **103** 1379–97
- [3] Merolla P A, Arthur J V., Alvarez-Icaza R, Cassidy A S, Sawada J, Akopyan F, Jackson B L, Imam N, Guo C, Nakamura Y, Brezzo B, Vo I, Esser S K, Appuswamy R, Taba B, Amir A, Flickner M D, Risk W P, Manohar R and Modha D S 2014 A million spiking-neuron integrated circuit with a scalable communication network and interface *Science (80-.)*. **345** 668–73
- [4] Torrejon J, Riou M, Araujo F A, Tsunegi S, Khalsa G, Querlioz D, Bortolotti P, Cros V, Yakushiji K, Fukushima A, Kubota H, Yuasa S, Stiles M D and Grollier J 2017 Neuromorphic computing with nanoscale spintronic oscillators *Nature* **547** 428–31
- [5] Yu S 2017 *Neuro-inspired Computing Using Resistive Synaptic Devices* (Cham: Springer International Publishing)
- [6] Qiao N, Mostafa H, Corradi F, Osswald M, Stefanini F, Sumislawska D and Indiveri G 2015 A reconfigurable on-line learning spiking neuromorphic processor comprising 256 neurons and 128K synapses *Front. Neurosci.* **9**
- [7] Grollier J, Querlioz D and Stiles M D 2016 Spintronic Nanodevices for Bioinspired

- [8] Sengupta A, Al Azim Z, Fong X and Roy K 2015 Spin-orbit torque induced spike-timing dependent plasticity *Appl. Phys. Lett.* **106**
- [9] Sengupta A and Roy K 2017 Encoding neural and synaptic functionalities in electron spin: A pathway to efficient neuromorphic computing *Appl. Phys. Rev.* **4**
- [10] Biswas A K, Atulasimha J and Bandyopadhyay S 2015 Straintronic spin-neuron *Nanotechnology* **26** 285201
- [11] Camsari K Y, Salahuddin S and Datta S 2017 Implementing p-bits with Embedded MTJ *IEEE Electron Device Lett.* **38** 1767–70
- [12] Pufall M R, Rippard W H, Csaba G, Nikonov D E, Bourianoff G I and Porod W 2015 Physical Implementation of Coherently Coupled Oscillator Networks *IEEE J. Explor. Solid-State Comput. Devices Circuits* **1** 76–84
- [13] Fukami S, Borders W A, Kurenkov A, Zhang C, DuttaGupta S and Ohno H 2017 Use of analog spintronics device in performing neuro-morphic computing functions *2017 Fifth Berkeley Symposium on Energy Efficient Electronic Systems & Steep Transistors Workshop (E3S)* (IEEE) pp 1–3
- [14] Khymyn R, Lisenkov I, Voorheis J, Sulymenko O, Prokopenko O, Tiberkevich V, Akerman J and Slavin A Ultra-fast artificial neuron: generation of picosecond-duration spikes in a current-driven antiferromagnetic auto-oscillator
- [15] Abbott L F 1999 Lopicque’s introduction of the integrate-and-fire model neuron (1907) *Brain Res. Bull.* **50** 303–4
- [16] Hutcheon B, Miura R M and Puil E 1996 Subthreshold membrane resonance in neocortical neurons. *J. Neurophysiol.* **76** 683–97
- [17] Llinas R R, Grace A A and Yarom Y 1991 In vitro neurons in mammalian cortical layer 4 exhibit intrinsic oscillatory activity in the 10- to 50-Hz frequency range. *Proc. Natl. Acad. Sci.* **88** 897–901
- [18] Pedroarena C and Llinás R 1997 Dendritic calcium conductances generate high-frequency oscillation in thalamocortical neurons. *Proc. Natl. Acad. Sci. U. S. A.* **94** 724–8
- [19] Llinás R R 1988 The intrinsic electrophysiological properties of mammalian neurons: insights into central nervous system function. *Science* **242** 1654–64
- [20] Izhikevich E M 2001 Resonate-and-fire neurons *Neural Networks* **14** 883–94
- [21] Nikonov D E, Csaba G, Porod W, Shibata T, Voils D, Hammerstrom D, Young I A and Bourianoff G I 2015 Coupled-Oscillator Associative Memory Array Operation for Pattern Recognition *IEEE J. Explor. Solid-State Comput. Devices Circuits* **1** 85–93
- [22] Hoppensteadt F C and Izhikevich E M 1999 Oscillatory neurocomputers with dynamic connectivity *Phys. Rev. Lett.* **82** 2983–6
- [23] Vodenicarevic D, Locatelli N, Abreu Araujo F, Grollier J and Querlioz D 2017 A

Nanotechnology-Ready Computing Scheme based on a Weakly Coupled Oscillator Network *Sci. Rep.* **7**

- [24] ITOH M and CHUA L O 2004 Star Cellular Neural Networks for Associative and Dynamic Memories *Int. J. Bifurc. Chaos* **14** 1725–72
- [25] Rössler U K, Bogdanov a N and Pfeleiderer C 2006 Spontaneous skyrmion ground states in magnetic metals. *Nature* **442** 797–801
- [26] Yu X Z, Onose Y, Kanazawa N, Park J H, Han J H, Matsui Y, Nagaosa N and Tokura Y 2010 Real-space observation of a two-dimensional skyrmion crystal. *Nature* **465** 901–4
- [27] Fert A, Cros V and Sampaio J 2013 Skyrmions on the track *Nat. Nanotechnol.* **8** 152–6
- [28] Yu X Z, Kanazawa N, Zhang W Z, Nagai T, Hara T, Kimoto K, Matsui Y, Onose Y and Tokura Y 2012 Skyrmion flow near room temperature in an ultralow current density *Nat. Commun.* **3** 988
- [29] Bhattacharya D, Al-Rashid M M and Atulasimha J 2016 Voltage controlled core reversal of fixed magnetic skyrmions without a magnetic field *Sci. Rep.* **6**
- [30] Nakatani Y, Hayashi M, Kanai S, Fukami S and Ohno H 2016 Electric field control of Skyrmions in magnetic nanodisks *Appl. Phys. Lett.* **108**
- [31] Zhang X, Ezawa M and Zhou Y 2015 Magnetic skyrmion logic gates: conversion, duplication and merging of skyrmions. *Sci. Rep.* **5** 9400
- [32] Tomasello R, Martinez E, Zivieri R, Torres L, Carpentieri M and Finocchio G 2014 A strategy for the design of skyrmion racetrack memories. *Sci. Rep.* **4** 6784
- [33] Ma X, Yu G, Razavi S A, Sasaki S S, Li X, Hao K, Tolbert S H, Wang K L and Li X 2017 Dzyaloshinskii-Moriya Interaction across an Antiferromagnet-Ferromagnet Interface *Phys. Rev. Lett.* **119**
- [34] Kang W, Huang Y, Zhang X, Zhou Y and Zhao W 2016 Skyrmion-Electronics: An Overview and Outlook *Proc. IEEE* **104** 2040–61
- [35] Pinna D, Araujo F A, Kim J-V, Cros V, Querlioz D, Bessiere P, Droulez J and Grollier J 2018 Skyrmion Gas Manipulation for Probabilistic Computing *Phys. Rev. Appl.* 1–41
- [36] Chen X, Kang W, Zhu D, Zhang X, Lei N, Zhang Y, Zhou Y and Zhao W 2018 A compact skyrmionic leaky–integrate–fire spiking neuron device *Nanoscale*
- [37] Li S, Kang W, Huang Y, Zhang X, Zhou Y and Zhao W 2017 Magnetic skyrmion-based artificial neuron device *Nanotechnology* **28**
- [38] Huang Y, Kang W, Zhang X, Zhou Y and Zhao W 2017 Magnetic skyrmion-based synaptic devices *Nanotechnology* **28**
- [39] He Z and Fan D 2017 A tunable magnetic skyrmion neuron cluster for energy efficient artificial neural network *Proceedings of the 2017 Design, Automation and Test in Europe, DATE 2017* pp 350–5
- [40] Bhattacharya D, Al-Rashid M M and Atulasimha J 2017 Energy efficient and fast

reversal of a fixed skyrmion two-terminal memory with spin current assisted by voltage controlled magnetic anisotropy *Nanotechnology* **28**

- [41] Bhattacharya D and Atulasimha J 2018 Skyrmion-Mediated Voltage-Controlled Switching of Ferromagnets for Reliable and Energy-Efficient Two-Terminal Memory *ACS Appl. Mater. Interfaces* **10** 17455–62
- [42] Amiri P K and Wang K L 2012 Voltage-Controlled Magnetic Anisotropy in Spintronic Devices *Spin* **2** 1240002
- [43] Niranjana M K, Duan C G, Jaswal S S and Tsymbal E Y 2010 Electric field effect on magnetization at the Fe/MgO(001) interface *Appl. Phys. Lett.* **96**
- [44] Maruyama T, Shiota Y, Nozaki T, Ohta K, Toda N, Mizuguchi M, Tulapurkar A A, Shinjo T, Shiraishi M, Mizukami S, Ando Y and Suzuki Y 2009 Large voltage-induced magnetic anisotropy change in a few atomic layers of iron *Nat. Nanotechnol.* **4** 158–61
- [45] Cui J, Liang C Y, Paisley E A, Sepulveda A, Ihlefeld J F, Carman G P and Lynch C S 2015 Generation of localized strain in a thin film piezoelectric to control individual magnetoelectric heterostructures *Appl. Phys. Lett.* **107**
- [46] Roy K, Bandyopadhyay S and Atulasimha J 2011 Hybrid spintronics and straintronics: A magnetic technology for ultra low energy computing and signal processing *Appl. Phys. Lett.* **99**
- [47] Grezes C, Lee H, Lee A, Wang S, Ebrahimi F, Li X, Wong K, Katine J A, Ocker B, Langer J, Gupta P, Khalili Amiri P and Wang K L 2017 Write Error Rate and Read Disturbance in Electric-Field-Controlled Magnetic Random-Access Memory *IEEE Magn. Lett.* **8**
- [48] Vansteenkiste A, Leliaert J, Dvornik M, Helsen M, Garcia-Sanchez F and Van Waeyenbergh B 2014 The design and verification of MuMax3 *AIP Adv.* **4**
- [49] Bandiera S, Sousa R C, Dahmane Y, Ducruet C, Portemont C, Baltz V, Auffret S, Prejbeanu I L and Dieny B 2010 Comparison of synthetic antiferromagnets and hard ferromagnets as reference layer in magnetic tunnel junctions with perpendicular magnetic anisotropy *IEEE Magn. Lett.* **1** 1–4
- [50] Nozaki T, Koziol-Rachwał A, Skowroński W, Zayets V, Shiota Y, Tamaru S, Kubota H, Fukushima A, Yuasa S and Suzuki Y 2016 Large Voltage-Induced Changes in the Perpendicular Magnetic Anisotropy of an MgO-Based Tunnel Junction with an Ultrathin Fe Layer *Phys. Rev. Appl.* **5**
- [51] Ong P V., Kioussis N, Amiri P K and Wang K L 2016 Electric-field-driven magnetization switching and nonlinear magnetoelasticity in Au/FeCo/MgO heterostructures *Sci. Rep.* **6**
- [52] Ho I-C, Xu Y and Mackenzie J D 1997 Electrical and optical properties of MgO thin film prepared by sol-gel technique *J. Sol-Gel Sci. Technol.* **9** 295–301
- [53] Yu G, Wang Z, Abolfath-Beygi M, He C, Li X, Wong K L, Nordeen P, Wu H, Carman G P, Han X, Alhomoudi I A, Amiri P K and Wang K L 2015 Strain-induced modulation of perpendicular magnetic anisotropy in Ta/CoFeB/MgO structures investigated by

ferromagnetic resonance *Appl. Phys. Lett.* **106**

- [54] Clark A E, Restorff J B, Wun-Fogle M, Lograsso T A and Schlagel D L 2000 Magnetostrictive properties of body-centered cubic Fe-Ga and Fe-Ga-Al alloys *IEEE Transactions on Magnetics* vol 36 pp 3238–40
- [55] Abbundi R and Clark A E 1977 Anomalous thermal expansion and magnetostriction of single crystal Tb₂₇Dy₇₃Fe₂ *IEEE Trans. Magn.* **13** 1519–20
- [56] Schatz F, Hirscher M, Schnell M, Flik G and Kronmüller H 1994 Magnetic anisotropy and giant magnetostriction of amorphous TbDyFe films *J. Appl. Phys.* **76** 5380–2
- [57] Theis, Wong T 2016 The End of Moore's Law: A New Beginning for Information Technology 41–50
- [58] Arthur J V. and Boahen K A 2011 Silicon-neuron design: A dynamical systems approach *IEEE Trans. Circuits Syst. I Regul. Pap.* **58** 1034–43